Néel-Type Skyrmion Lattice in the Tetragonal Polar Magnet $VOSe_2O_5$

Takashi Kurumaji,[1,*] Taro Nakajima,[1] Victor Ukleev,[1] Artem Feoktystov,[2] Taka-hisa Arima,[1,3] Kazuhisa Kakurai,[1,4] and Yoshinori Tokura[1,5]

[1]*RIKEN Center for Emergent Matter Science (CEMS), Wako 351-0198, Japan*
[2]*Forschungszentrum Jülich GmbH, Jülich Centre for Neutron Science (JCNS) at Heinz Maier-Leibnitz Zentrum (MLZ), Garching 85748, Germany*
[3]*Department of Advanced Materials Science, The University of Tokyo, Kashiwa 277-8561, Japan*
[4]*CROSS-Tokai, Research Center for Neutron Science and Technology, Tokai, Ibaraki 319-1106, Japan*
[5]*Department of Applied Physics, The University of Tokyo, Tokyo 113-8656, Japan*

(Received 12 July 2017; published 4 December 2017)

The formation of the triangular Skyrmion lattice is found in a tetragonal polar magnet $VOSe_2O_5$. By magnetization and small-angle neutron scattering measurements on the single crystals, we identify a cycloidal spin state at zero field and a Néel-type Skyrmion-lattice phase under a magnetic field along the polar axis. Adjacent to this phase, another magnetic phase of an incommensurate spin texture is identified at lower temperatures, tentatively assigned to a square Skyrmion-lattice phase. These findings exemplify the versatile features of Néel-type Skyrmions in bulk materials, and provide a further opportunity to explore the physics of topological spin textures in polar magnets.

DOI: 10.1103/PhysRevLett.119.237201

Skyrmions have been investigated in various magnetic systems [1–5], especially noncentrosymmetric magnets, where the topological spin textures are stabilized by Dzyaloshinskii-Moriya (DM) interaction due to the relativistic spin-orbit coupling [6–9] under an applied magnetic field (H). A periodic lattice of Skyrmions is typically found in chiral magnets such as B20 alloys [1,2,10], multiferroic Cu_2OSeO_3 [11], and β-Mn-type CoZnMn alloys [12], where the Skyrmion form Bloch-type, whirl-like spin vortex structure. Early theoretical predictions [8,9] and subsequent experiment [13], however, revealed that a different type of Skyrmion emerges due to another kind of asymmetry of the underlying lattice. Polar systems exemplify one such noncentrosymmetry, in which DM interaction confines the magnetic modulation direction vector ($\vec{q}$) perpendicular to the polar axis to stabilize the cycloidal spin order, as shown in Fig. 1(a). In this case, H applied parallel to the polar (c) axis induces the Néel-type Skyrmion as shown in Fig. 1(b): the spin rotates outwards from the core of the vortex.

The Néel-type Skyrmion has been frequently observed in magnetic ultrathin films and multilayers affected by DM interaction via broken inversion symmetry at the interface [3,4,14–16], which provide an important arena for practical applications in spintronics devices. In this context, a precise understanding of Néel-type Skyrmions and related spin textures by targeting a bulk polar magnet is of potential importance as the foundation for Skyrmion device research. However, the Skyrmion lattice (SkL) phase in polar bulk magnets has not been fully investigated, except for a lacunar spinel compound [13] with trigonal crystal structure. In order to gain insights on the physical origin and the stability of Skyrmion and related spin textures in a noncentrosymmetric magnet, expansion of material classes of bulk polar magnets hosting Néel-type SkL is desired.

We have investigated the tetragonal polar magnet, $VOSe_2O_5$, which belongs to the C_{4v} point group satisfying the prerequisite for hosting the Néel Skyrmion [8]. Its crystal structure [Fig. 1(c)] consists of stacked square lattices of VO_5 tetragonal pyramids [17], each of which carries a magnetic V^{4+} ion with spin-1/2 moment. Previous works [18,19] reported Curie temperature (T_C) of ~8 K and the field-induced saturated magnetization, ~0.47 μ_B/f.u., at the lowest temperature. The density functional calculation in Ref. [19] suggested a 3-up-1-down type ferrimagnetic spin

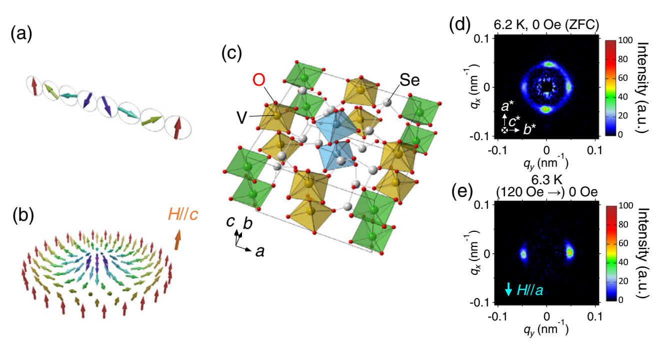

FIG. 1. Schematic spin configuration of (a) cycloidal spiral order and (b) a Néel-type Skyrmion under magnetic field (H) along the c axis. (c) Crystal structure of $VOSe_2O_5$. Blue, green, and yellow tetragonal pyramids are inequivalent VO_5 polyhedra in a unit cell. Small-angle neutron scattering (SANS) pattern for the coaligned single crystals in zero field at 6.2 K (±0.1 K), (d) after the ZFC procedure, and (e) after the field-trained process with $H = 120$ Oe. H is perpendicular to the incident neutron beam. The incident beam is parallel to the c axis.

ground state, which predicts spontaneous magnetization 0.5 μ_B/f.u.. Nevertheless, some anomalies in magnetic susceptibility have remained unidentified, implying nontrivial magnetism in this compound [18,19].

In this single-crystal study, we performed measurements of magnetization and small-angle neutron scattering (SANS) to unveil the magnetic phases, including a triangular SkL phase under $H\|c$, as well as the cycloidal spin order propagating perpendicular to the polar axis in zero field. We found that the triangular SkL competes with versatile magnetic phases, one of which is distinct from the cycloidal or collinear spin state, but shows magnetic modulation with the fourfold symmetric SANS pattern under $H\|c$. We compared our results with the recently discovered Néel-SkL in trigonal GaV_4S_8 [13] to gain insights on the stable topological spin textures possible in a polar magnet.

Single crystals of $VOSe_2O_5$ were grown by chemical vapor transport reaction with NH_4Cl [20]. Sizes of the obtained single crystals were typically $0.5 \times 0.5 \times 0.7$ mm^3. Magnetization and ac magnetic susceptibility were measured by a superconducting quantum interference device magnetometer (MPMS3, Quantum Design). To measure ac susceptibility, typically a 1 Oe ac field at 100 Hz was applied along the dc H direction. During the H scan measurement, such as in Fig. 2, the temperature precision is better than ± 0.01 K. SANS measurements were performed at the KWS-1 beam line at Heinz Maier-Leibnitz Zentrum (MLZ), Garching, Germany [20–22]. We employed twenty-seven pieces of crystals (total volume of 4.6 mm^3), which were carefully coaligned on an aluminum plate with the same crystallographic orientation [20]. The sample on the Al plate was mounted into a ^{3}He-circulation refrigerator with its [001] direction parallel to the incident beam. A magnetic field parallel or perpendicular to the incident beam was generated by an electromagnet. To avoid the effect of residual fields, the electromagnet was demagnetized before performing subsequent zero or applied field experiments.

In the SANS pattern [Fig. 1(d)] for the coaligned single crystals at 6.2 K in zero field with the incident neutron beam parallel to the c axis, we observed the in-plane magnetic modulation, which was perhaps hidden behind the nuclear scattering in the previous work [19]. Four clear magnetic Bragg reflections are observed at $q = 0.046$ nm^{-1} along the crystallographically equivalent a and b axes, suggesting the multidomain nature of the single-q state for $\vec{q}\|\vec{a}$ and $\vec{q}\|\vec{b}$. We further find that a single-q domain can be selected with in-plane H. Figure 1(e) shows the zero-field SANS pattern at 6.3 K after a field-trained procedure with $H = 120$ Oe along the a axis [20]. Two out of four Bragg reflections satisfying the $\vec{q}\perp\vec{H}$ configuration are observed, which is consistent with the anticipated cycloidal spin structure [23]. This result indicates that the spin modulation in this system obeys the DM interaction for the polar symmetry, which determines the Néel-type spin configuration as the stable Skyrmion form under $H//c$.

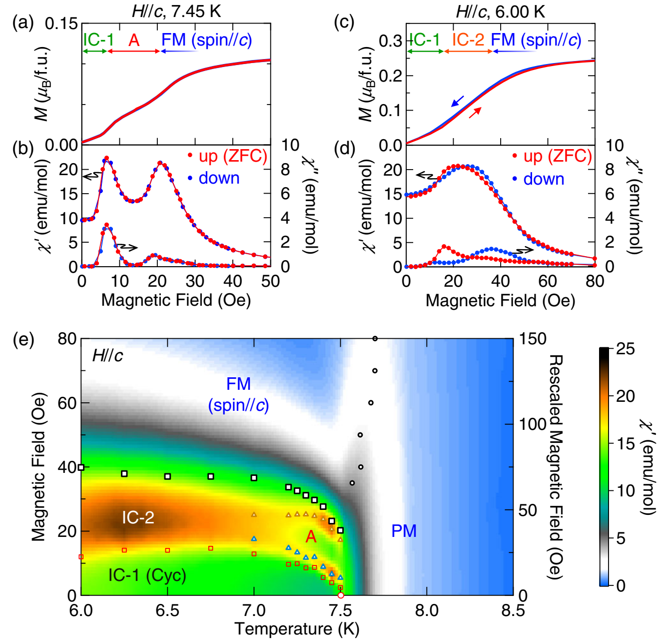

FIG. 2. (a)–(d) H dependence of M, χ', and χ'' under $H//c$ at (a),(b) 7.45 K, and (c),(d) 6.00 K, respectively. Red (blue) circle is for the H-increasing (-decreasing) scan. The H-increasing scan was performed after the ZFC procedure. (e) Color plot of χ' for $H//c$, and the magnetic phase diagram determined by the measurements of M, χ', and χ'', where each magnetic phase is indicated as paramagnetic (PM); FM (3-up-1-down type state with spin$//c$); cycloidal IC-1 (Cyc); incommensurately modulated magnetic order (IC-2) (likely square Skyrmion lattice state, see the text); and triangular Skyrmion lattice state (A). Open circles are the peak in the χ'-T curve; open triangles show the peak in the χ'-H curve; and open squares show the peak in the $(d\chi'/dH)$-H curve. Rescaled H for the phase diagram of the assembled-crystals sample for the SANS investigation is shown on the right ordinate.

The magnetic transition from the cycloidal spin phase to the SkL phase, or the so-called A phase, under $H\|c$ is exemplified by the two-step metamagnetic transition in magnetization (M) at 7.45 K [Fig. 2(a)], near $T_C = 7.50$ K. This is a common feature of SkL formation, as observed in various Skyrmion-hosting compounds [11,13,24,25]. We identify the A-phase boundary by the double-peak structure in both the real (χ') and imaginary (χ'') parts of the ac magnetic susceptibility [Fig. 2(b)]. This χ'-valley region disappears at slightly lower temperature ($T < 7.20$ K). However, at 6.00 K [Figs. 2(c)–2(d)], H-dependence of M and χ' still show nonmonotonic behavior around 15 Oe. This phase transition is of first-order nature, as the peak for χ'' suggests dissipation due to the motion of a domain wall separating the cycloidal state and distinct magnetic states, IC-1 and IC-2, respectively [top abscissa in Fig. 2(c)]. Here, the notation, IC, stands for an incommensurate magnetic

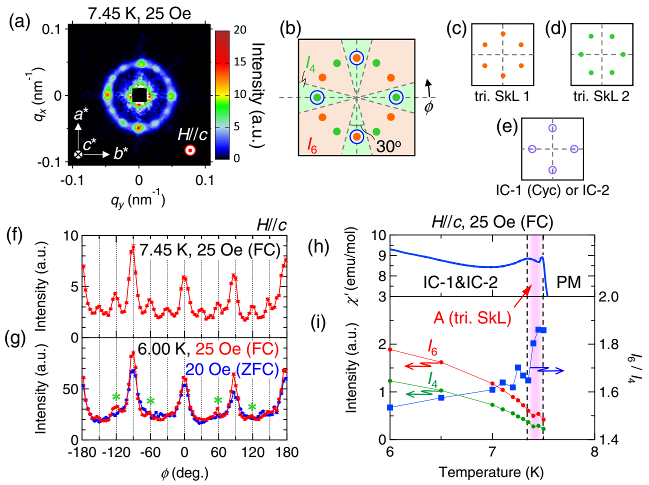

FIG. 3. (a) SANS pattern for the coaligned single crystals at 7.45 K with $H = 25$ Oe along the c axis. H and the incident neutron beam are parallel with each other and both along the c axis. (b) Schematic illustration of the SANS pattern for (a). Blue, green, and orange circles indicate the respective Bragg spots corresponding to the magnetic orders shown in (c),(d), and (e). Integration sectors for the intensity of magnetic fourfold spots (green region) I_4 and SkL (red region) I_6. Definition of the azimuth angle (ϕ) is also indicated. (c)–(e) Schematics of the SANS pattern for (c),(d), two kinds of domain of triangular SkL and (e) fourfold pattern for multidomain of cycloidal order in the IC-1 phase or for the IC-2 phase. (f),(g) ϕ dependence of integrated intensity for the field-cooling (FC) process with 25 Oe for $H//c$ at (f) 7.45, and (g) 6.00 K (red circle). In (g), the data with 20 Oe for $H//c$ after the ZFC procedure are also plotted by blue circles. The intensity integration is done over the radial $|\vec{q}|$ range $0.038 \leq |\vec{q}| \leq 0.056\ \mathrm{nm}^{-1}$ for 7.45 K, and $0.036 \leq |\vec{q}| \leq 0.053\ \mathrm{nm}^{-1}$ for 6.00 K. The remnant intensity peaks for a super cooled component of the triangular SkL state are indicated by asterisks. (h),(i) Temperature dependence of (h) χ', (i) I_4, I_6, and their ratio I_6/I_4 for the field-cooling process with 25 Oe for $H//c$.

order, which is confirmed by the SANS investigation as mentioned earlier and below. Figure 2(e) is the magnetic phase diagram for $H \| c$, determined from the magnetization measurement, with the color plot of χ'. A pocketlike magnetic phase around T_C with a finite field (as indicated by A) is clearly identified, as well as the IC-2 phase in a lower temperature region.

The triangular SkL formation in the A phase is identified by a 12-fold SANS pattern in the configuration with H parallel to both the c axis and the neutron beam. Figure 3(a) shows the SANS pattern at 7.45 K with $H = 25$ Oe along the c axis. Note here that the A-phase region for the SANS sample exists in a higher H region than that for Fig. 2(a) due to the sample-shape-dependent difference of demagnetization fields; see rescaled H at the right ordinate in Fig. 2(e)[20]. We took a constant-field path with decreasing temperature from the paramagnetic state to the A phase. Besides four Bragg reflections along the a and b axes, additional spots show up [Fig. 3(a)] at the positions irrelevant to the tetragonal symmetry. The schematic SANS pattern is shown in Fig. 3(b), which can be addressed to the superposition of three SANS patterns as Figs. 3(c)–3(e). Among them, Figs. 3(c) and 3(d) show two types of the triangular SkL state with 90° rotation from each other, in which one q of the triple-q structure is fixed along the a [Fig. 3(c)] or b [Fig. 3(d)] axis, respectively. As shown by the azimuthal angle (ϕ) dependence of the integrated intensity in Fig. 3(f), the separated spots with the 30° period clearly reflect the hexagonal symmetry of the superposing spin textures. Similar 12-fold SANS patterns due to a multidomain state of the triangular SkL have been reported in other Skyrmion-hosting materials such as the CoZnMn alloy [26] and Cu_2OSeO_3 [27] under H along the [001] axis, similarly to the present case. Superposition with a fourfold pattern [Fig. 3(e)] appears to be due to the coexisting IC-1 and/or IC-2 states because the assembled single crystals for the SANS investigation effectively experience an inhomogeneous magnetic field due to the different demagnetization effect for individual pieces.

It is confirmed that further cooling destructs this 12-fold SANS pattern for the triangular SkL state. As shown by the red circle in Fig. 3(g), when cooled to 6.00 K with $H = 25$ Oe [Fig. 3(g)], the 12-fold intensity profile evolves into four peaks with 90° period, in accord with the formation of the IC-1 and IC-2 phase domains. Note that weak peaks, indicated by asterisks in Fig. 3(g), involving the triangular SkL are observed at 6.00 K. This suggests that a small portion of the triangular SkL state for Fig. 3(d) remains in a supercooled metastable state, as has been identified in other SkL materials [26,28,29]. The remnant SkL peaks were not observed in the SANS pattern for $H =$ 20 Oe (or 30 Oe) at 6.00 K in the H-increasing process after the zero-field cooling (ZFC) procedure [Fig. 3(g)], which suggests the metastability of these remnant SkL structures. Note that the SANS measurement offers the reciprocal-space image of the spin texture. Further investigation by the real space observation technique is desired for more concrete proofs of the spin texture, such as the two-domain state of the SkLs and the quenched SkL state at lower temperatures coexisting with IC-1/IC-2 states.

To connect the A-phase region identified by the magnetic susceptibility measurement and the 12-fold SANS pattern, we performed further analysis on the SANS intensity for each spin state. We partitioned the reciprocal plane as shown in Fig. 3(b) to plot the temperature dependence of each integrated intensity in Fig. 3(i): the intensity for the fourfold pattern (I_4) and that of the diagonal region (I_6) representing contribution originating from the triangular SkL. Here, I_6 is scaled by 3/2 to compare the intensity of individual peaks. Both I_4 and I_6 increase as the temperature decreases in accord with the thermal evolution of the spin moment. The intensity in the I_6 region originates from the following two components: (i) the broadened Bragg spots in the I_4 region due to flexibility of the q vector for the

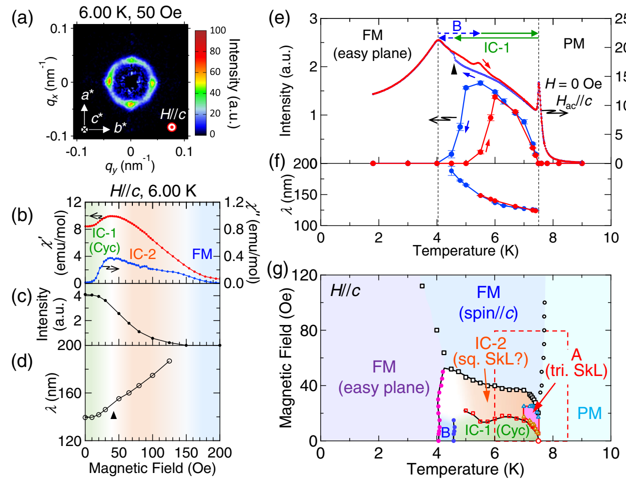

FIG. 4. (a) SANS pattern for the coaligned single crystals at 6.00 K with 50 Oe for $H//c$. H and the incident neutron beam are parallel to each other and both are along the c axis. (b)–(d) H dependence of (b) χ' and χ'', (c) integrated SANS intensity for the overall detector surface, and (d) the wavelength λ of the magnetic modulation. (e),(f) Temperature dependence of the respective data measured in zero field for a cooling (blue circles) scan and a heating scan (red circles): (e) the SANS integrated intensity and χ'Unhandled Math Content: Z with the ac magnetic field H_{ac} along the c axis, and (f) λ measured by the SANS pattern with the neutron beam parallel to the c axis. (g) Magnetic phase diagram of $VOSe_2O_5$ determined by magnetization measurements with $H//c$. Phase boundaries for the white region (~4.5 K, ~30 Oe) could not be definitely determined by the magnetization measurements. For the definition of each symbol, see the caption for Fig. 2(e). Red dashed square indicates the H-T region shown in Fig. 2(e).

in-plane direction; (ii) the supercooled triangular SkL state. To renormalize the thermal increase of I_6, we plotted the relative intensity I_6/I_4 for the right ordinate in Fig. 3(i). I_6/I_4 peaks in the triangular SkL region between χ' peaks [Fig. 3(h)], pink hatching, then decays with decreasing temperature to a finite value. These results support that the A-phase region of the phase diagram is occupied by the thermally equilibrium triangular SkL state.

Note that the presence of the IC-2 phase is unique in the present tetragonal system; in the trigonal Néel-Skyrmion material GaV_4S_8, the triangular SkL phase is in proximity with the cycloidal, ferromagnetic, and paramagnetic phases [13]. A typical SANS pattern for the IC-2 phase taken at 6.00 K with $H = 50$ Oe along the c axis after the ZFC procedure is shown in Fig. 4(a) [see the rescaled H in Fig. 2(e)]. Clear fourfold Bragg reflections along the a and b axes can be observed. To identify the magnetic transition between the IC-1 and IC-2 states, we show the H dependence of the integrated intensity and wavelength (λ) of the magnetic modulation together with χ' and χ'' measured for the assembled-crystals sample (SANS sample) [Figs. 4(b)–4(d)]. Although the integrated intensity monotonically wanes towards the ferrimagnetic (FM) phase, λ shows a discernible kink at ~40 Oe as indicated by a triangle [Fig. 4(d)], which correlates with features in χ' and χ'' [Fig. 4(b)]. This suggests that the IC-2 phase has in-plane magnetic modulation while being distinct from the cycloidal spin order (IC-1), or any other spin order such as a chiral soliton lattice state [30] continuously evolved from IC-1 under $H\|c$.

The enriched magnetic phase diagram for this system is also exemplified by the thermal evolution of the SANS integrated intensity for the IC-1 state in zero field as shown in Fig. 4(e). The intensity increases as the temperature decreases from T_C until a collapse occurring at ~4.5 K. This successive transition was previously suggested by the ac susceptibility measurement using powder sample [19]. We measured the temperature dependence of χ' in zero field using the single crystal for the ac magnetic field (H_{ac}) parallel to the c axis [Fig. 4(e)]. Note that the disappearance of SANS intensity does not correlate with the drop of χ' at 4.0 K, which we assigned to the transition to the FM ($q = 0$) ground state, but with the anomaly at 4.5 K as indicated by a black triangle in Fig. 4(e). The hysteresis in the temperature dependence of the SANS intensity and χ' around 5 K indicates the presence of the other magnetic phase (B phase) between the IC-1 and the ground state. Figure 4(g) summarizes the H-T phase diagram. IC-1 and IC-2 are restricted to a limited temperature range (4.0 K $< T <$ 7.5 K), due to the transition into the B phase and the FM state at lower temperatures. The saturation magnetic field under $H\|c$ [Fig. 4(g), open squares] rapidly increases with lowering temperature, which suggests the easy-plane type anisotropy for the FM ground state. The nature of the magnetic structure of the B phase is not fully clear, but a plausible candidate is a commensurate ($q = 0$) canted order, which may be derived by the diverging tendency of λ as observed in Fig. 4(f) prior to entering the easy-plane ground state.

The increase in λ for IC-1 with decreasing temperature [Fig. 4(f)] suggests the thermal variation of the magnitude of symmetric and antisymmetric (DM) exchange interactions, and the magnetic anisotropy of the present multisublattice system. The role of such parameters for stable spin textures in a polar system under a magnetic field has been discussed with various computational approaches [31–34]. Several theoretical studies predicted that a polar magnet, in contrast to a chiral magnet, could have versatile magnetic phases, including the square SkL state under H, which is more stable than the triangular SkL state in the presence of easy plane anisotropy [31,33,34]. Note that the tetragonal anisotropy may also be relevant in the present system since the q vector for the cycloidal spin order is weakly locked along the a or b axis [Fig. 1(d)] in zero field, in contrast to the homogeneous ring observed at the SANS pattern in the case of the trigonal GaV_4S_8 [23]. Although the formation of a multiple-q state in the IC-2 phase remains elusive within the present experimental information, a square SkL state is a plausible candidate under the interplay between the thermally changing uniaxial and tetragonal magnetic anisotropies originating from the underlying crystal structure. Further theoretical and experimental studies are needed to clarify the stable spin texture in this unique tetragonal polar magnet.

In conclusion, we experimentally identified the triangular Skyrmion lattice (SkL) phase in a tetragonal polar system $VOSe_2O_5$. Cycloidal spin modulation in the zero field evidences the stability of the Néel-type Skyrmion in the present system. We unraveled the relation between the triangular SkL state and the other magnetic phase with in-plane modulation at low temperature under $H \| c$. This phase is different from the cycloidal spin order in zero field, and possibly a square SkL state induced by the interplay of the tetragonal crystal anisotropy and the effect of thermally varying uniaxial anisotropy. This system shows a distinct magnetic correlation with the recently discovered trigonal polar Skyrmion material, providing novel insights into the stabilization of SkL states in polar magnets.

The authors thank D. Hashizume for support for administration and operation of a single-crystal x-ray diffractometer; Dr. T. Reimann, M. Seifert, and Dr. M. Schulz for providing us the magnet and helping with its operation. We also thank X. Z. Yu, D. Morikawa, T. Matsumoto, Y. Tokunaga, I. Kezsmarki, M. Kriener, and L. Ye for enlightening discussions. This research was supported in part by JSPS Grant-In-Aid for Scientific Research(S) No. 24224009, and Grant-In-Aid for Young Scientists(B) No. 17K14351. One of the authors (K. K.) acknowledges the support by the Helmholtz International Fellow Award.

*Corresponding author.
takashi.kurumaji@riken.jp

[1] S. Mühlbauer, B. Binz, F. Jonietz, C. Pfleiderer, A. Rosch, A. Neubauer, R. Georgii, and P. Boni, Science **323**, 915 (2009).
[2] X. Z. Yu, Y. Onose, N. Kanazawa, J. H. Park, J. H. Han, Y. Matsui, N. Nagaosa, and Y. Tokura, Nature (London) **465**, 901 (2010).
[3] S. Heinze, K. von Bergmann, M. Menzel, J. Brede, A. Kubetzka, R. Wiesendanger, G. Bihlmayer, and S. Blugel, Nat. Phys. **7**, 713 (2011).
[4] N. Romming, C. Hanneken, M. Menzel, J. E. Bickel, B. Wolter, K. Von Bergmann, A. Kubetzka, and R. Wiesendanger, Science **341**, 636 (2013).
[5] S. Gao, O. Zaharko, V. Tsurkan, Y. Su, J. S. White, G. S. Tucker, B. Roessli, F. Baurdarot, R. Sibille, D. Chernyshov, T. Fennell, A. Loidl, and C. Ruegg, Nat. Phys. **13**, 157 (2017).
[6] I. Dzyaloshinskii, J. Phys. Chem. Solids **4**, 241 (1958).
[7] T. Moriya, Phys. Rev. **120**, 91 (1960).
[8] A. N. Bogdanov and D. A. Yablonskii, Sov. Phys. JETP **68**, 101 (1989).
[9] A. Bogdanov and A. Hubert, J. Magn. Magn. Mater. **138**, 255 (1994).
[10] X. Z. Yu, N. Kanazawa, Y. Onose, K. Kimoto, W. Z. Zhang, S. Ishiwata, Y. Matsui, and Y. Tokura, Nat. Mater. **10**, 106 (2011).
[11] S. Seki, X. Z. Yu, S. Ishiwata, and Y. Tokura, Science **336**, 198 (2012).
[12] Y. Tokunaga, X. Z. Yu, J. S. White, H. M. Ronnow, D. Morikawa, Y. Taguchi, and Y. Tokura, Nat. Commun. **6**, 7638 (2015).
[13] I. Kezsmarki, S. Bordacs, P. Milde, E. Neuber, L. M. Eng, J. S. White, H. M. Ronnow, C. D. Dewhurst, M. Mochizuki, K. Yanai, H. Nakamura, D. Ehlers, V. Tsurkan, and A. Loidl, Nat. Mater. **14**, 1116 (2015).
[14] G. Chen, A. Mascaraque, A. T. N'Diaye, and A. K. Schmid, Appl. Phys. Lett. **106**, 242404 (2015).
[15] O. Boulle, J. Vogel, H. Yang, S. Pizzini, D. de S. Chaves *et al.*, Nat. Nanotechnol. **11**, 449 (2016).
[16] C. Moreau-Luchaire, C. Moutafis, N. Reyren, J. Sampaio, C. A. F. Vaz *et al.*, Nat. Nanotechnol. **11**, 444 (2016).
[17] P. G. Meunier, M. Bertaud, and J. Galy, Acta Crystallogr. Sect. B **30**, 2834 (1974).
[18] J.-C. Trombe, A. Gleizes, J. Galy, J.-P. Renard, Y. Journaux, and M. Verdaguer, Nouveau Journal de chimie **11**, 321 (1987).
[19] S.-H. Kim, P. S. Halasyamani, B. C. Melot, R. Seshadri, M. A. Green, A. S. Sefat, and D. Mandrus, Chem. Mater. **22**, 5074 (2010).
[20] See Supplemental Material at http://link.aps.org/supplemental/10.1103/PhysRevLett.119.237201 for an extended discussion, including Refs. [17,19,21,22].
[21] H. Maier-Leibnitz Zentrum *et al.*, J. Large-Scale Research Facilities **1**, A28 (2015).
[22] A. V. Feoktystov, H. Frielinghaus, Z. Di, S. Jaksch, V. Pipich, M.-S. Appavou, E. Babcock, R. Hanslik, R. Engels, G. Kemmerling, H. Kleines, A. Ioffe, D. Richter, and T. Bruckel, J. Appl. Crystallogr. **48**, 61 (2015).
[23] J. S. White, A. Butykai, R. Cubitt, D. Honecker, C. D. Dewhurst, L. F. Kiss, V. Tsurkan, and S. Bordacs, arXiv:1704.03621.
[24] A. Bauer and C. Pfleiderer, Phys. Rev. B **85**, 214418 (2012).
[25] H. Wilhelm, M. Baenitz, M. Schmidt, U. K. Rossler, A. A. Leonov, and A. N. Bogdanov, Phys. Rev. Lett. **107**, 127203 (2011).
[26] K. Karube, J. S. White, N. Reynolds, J. L. Gavilano, H. Oike, A. Kikkawa, F. Kagawa, Y. Tokunaga, H. M. Ronnow, Y. Tokura, and Y. Taguchi, Nat. Mater. **15**, 1237 (2016).
[27] K. Makino, J. D. Reim, D. Higashi, D. Okuyama, T. J. Sato, Y. Nambu, E. P. Gilbert, N. Booth, S. Seki, and Y. Tokura, Phys. Rev. B **95**, 134412 (2017).
[28] W. Munzer, A. Neubauer, T. Adams, S. Muhlbauer, C. Franz, F. Jonietz, R. Georgii, P. Boni, B. Pedersen, M. Schmidt, A. Rosch, and C. Pfleiderer, Phys. Rev. B **81**, 041203(R) (2010).
[29] H. Oike, A. Kikkawa, N. Kanazawa, Y. Taguchi, M. Kawasaki, Y. Tokura, and F. Kagawa, Nat. Phys. **12**, 62 (2016).
[30] Y. Togawa, Y. Kousaka, K. Inoue, and J.-I. Kishine, J. Phys. Soc. Jpn. **85**, 112001 (2016).
[31] S. D. Yi, S. Onoda, N. Nagaosa, and J. H. Han, Phys. Rev. B **80**, 054416 (2009).
[32] S. Banerjee, J. Rowland, O. Erten, and M. Randeria, Phys. Rev. X **4**, 031045 (2014).
[33] S.-Z. Lin, A. Saxena, and C. D. Batista, Phys. Rev. B **91**, 224407 (2015).
[34] J. Rowland, S. Banerjee, and M. Randeria, Phys. Rev. B **93**, 020404(R) (2016).